The FEBS Journal

FEBS PRESS science publishing by scientists

Deciphering the number and location of active sites in the monomeric glyoxalase I of *Zea mays*

Javier M. González[1], Romina B. Agostini[2], Clarisa E. Alvarez[2], Sebastián Klinke[3], Carlos S. Andreo[2] and Valeria A. Campos-Bermudez[2]

1 Instituto de Bionanotecnología del NOA (INBIONATEC-CONICET), Universidad Nacional de Santiago del Estero (UNSE), Argentina
2 Centro de Estudios Fotosintéticos y Bioquímicos (CEFOBI-CONICET), Universidad Nacional de Rosario, Argentina
3 Fundación Instituto Leloir, IIBBA-CONICET, Plataforma Argentina de Biología Estructural y Metabolómica PLABEM, Buenos Aires, Argentina

Keywords
glyoxalase I; hemithioacetal; maize; methylglyoxal; protein tunnel

Correspondence
J. M. González, Instituto de Bionanotecnología del NOA (INBIONATEC-CONICET), Universidad Nacional de Santiago del Estero (UNSE). RN9, Km1125, G4206XCP Santiago del Estero, Argentina
Tel: +54 93854238352
E-mail: javier.m.gonzalez.mail@gmail.com
V. A. Campos-Bermudez, Centro de Estudios Fotosintéticos y Bioquímicos (CEFOBI-CONICET), Universidad Nacional de Rosario. Suipacha 531, S2002LRK Rosario, Argentina
Tel: +54 93414371955, Ext. 112
Email: campos@cefobi-conicet.gov.ar

(Received 13 February 2019, revised 18 March 2019, accepted 15 April 2019)

doi:10.1111/febs.14855

Detoxification of methylglyoxal, a toxic by-product of central sugar metabolism, is a major issue for all forms of life. The glyoxalase pathway evolved to effectively convert methylglyoxal into D-lactate via a glutathione hemithioacetal intermediate. Recently, we have shown that the monomeric glyoxalase I from maize exhibits a symmetric fold with two cavities, potentially harboring two active sites, in analogy with homodimeric enzyme surrogates. Here we confirm that only one of the two cavities exhibits glyoxalase I activity and show that it adopts a tunnel-shaped structure upon substrate binding. Such conformational change gives rise to independent binding sites for glutathione and methylglyoxal in the same active site, with important implications for the molecular reaction mechanism, which has been a matter of debate for several decades.

Database
Structural data are available in The Protein Data Bank database under the accession numbers 6BNN, 6BNX, and 6BNZ.

Introduction

Methylglyoxal (MG) is a cytotoxic by-product of sugar metabolism. The major source of MG is the degradation of triose phosphates. A nonenzymatic deprotonation of the key glycolytic metabolites glyceraldehyde-3-phosphate and dihydroxyacetone phosphate leads to the formation of an enediol phosphate intermediate, and the spontaneous elimination of the phosphate group produces MG [1,2]. This elimination reaction also takes place during the reaction catalyzed by triose phosphate isomerase, where the enediol phosphate formed in the catalytic site of the enzyme can be released and rapidly converted into MG and inorganic phosphate [1,3,4]. MG is electrophilic and highly reactive toward varied cellular components, resulting in their irreversible modification and formation of adducts and cross-links collectively named advanced glycation end products [5]. The reaction of MG with DNA introduces nucleic acid strand breaks and

Abbreviations
*Zm*GLXI, *Zea mays* glyoxalase I; MG, methylglyoxal; GSH, glutathione; HTA, hemithioacetal; SLG, S-D-lactoylglutathione.

elevated mutation frequencies [6,7]. Reactions of MG with proteins, preferentially directed to arginine residues, lead to structural and functional changes [8].

The ubiquitous glyoxalase pathway evolved to effectively detoxify MG. The enzymes glyoxalase I (GLXI, S-D-lactoylglutathione lyase, EC 4.4.1.5) and glyoxalase II (GLXII, hydroxyacylglutathione hydrolase, EC 3.1.2.6) sequentially convert MG into D-lactate by means of two glutathione adduct intermediates, a hemithioacetal (HTA) and S-D-lactoylglutathione (SLG) (Fig. 1). Besides, a GSH-independent glyoxalase activity has been reported, named glyoxalase III [9]. In the conventionally established reaction mechanism, the HTA formed by spontaneous condensation of MG and GSH is isomerized into SLG by GLXI, which is later hydrolyzed into GSH and D-lactate by GLXII [10]. The glyoxalase system has been thoroughly studied in the animal kingdom and numerous roles for glyoxalases have been proposed, including its function in cell proliferation, embryogenesis, maturation, and cell death [11,12]. GLXI is an important target for clinical research, as diseases such as diabetes and hyperglycemia have been associated with increased MG levels [13,14]. Plants also accumulate MG from sugar metabolism, and this excess MG needs to be eliminated in order to maintain cell homeostasis [15]. The presence of glyoxalases in the plant kingdom was first reported in Douglas fir needles [16], and since then several studies reported its presence in both monocots and dicots [17–22]. The expression of glyoxalases in plants has been associated with various abiotic stress responses, and they have been suggested as biomarkers for stress tolerance [22]. We have previously characterized the *Zea mays* glyoxalase I (*Zm*GLXI), which presumably acts in the defense response of maize to fungal infections [23].

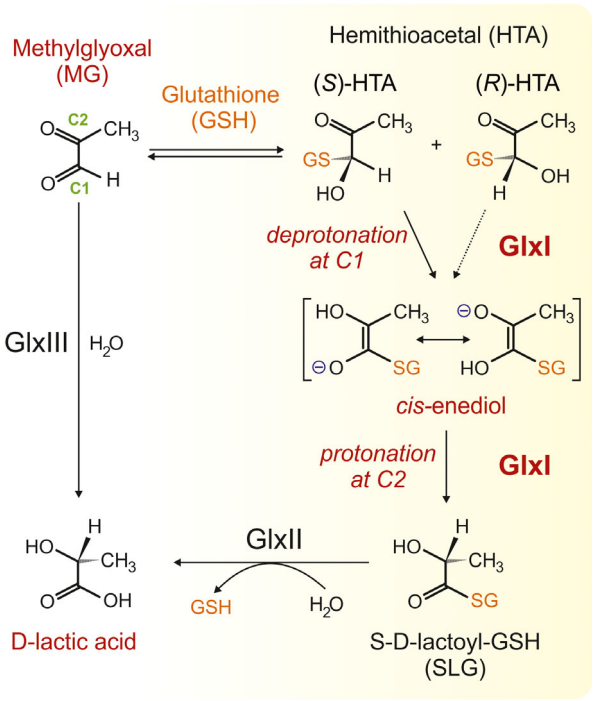

Fig. 1. The glyoxalase pathway. Glyoxalases I and II (GlxI and GlxII) detoxify methylglyoxal (MG) to D-lactate via an S-D-lactoylglutathione (SLG) intermediate. An alternative pathway involves a single enzyme, named GlxIII, which directly converts methylglyoxal (MG) to D-lactate, without the utilization of glutathione (GSH). Note that the proposed substrate of GlxI is the hemithioacetal (HTA) racemate resulting from reaction of MG and glutathione (GSH) in solution, but currently accepted mechanisms only explain the formation of diastereomer (*S*)-HTA [41].

Glyoxalase I requires Ni(II) or Zn(II) as cofactors [24–28], typically displaying an octahedral coordination geometry, with four conserved ligand residues present in H/E/Q/E or H/E/H/E metal-binding motifs, completed by two solvent molecules [23,29,30]. Most GLXI proteins characterized from prokaryotes have been found to be homodimeric, exhibiting two identical active sites [30]. However, monomeric forms of this enzyme harboring two active sites have also been described [31,32].

We have recently determined the first three-dimensional structure of a plant glyoxalase I (PDB 5D7Z) [23]. The *Zm*GLXI polypeptide folds into two domains, each with two βαβββ motifs, which render two wide cavities harboring the putative active sites, in a similar fashion to homodimeric surrogates. However, in *Zm*GLXI only one of the cavities exhibits the residues required for metal coordination (namely, site A: H96, E144, Q157, and E208), strongly suggesting that the enzyme has only one active site. Instead, the second cavity exhibits an incomplete metal coordination set that we named site B, with V278 replacing a conserved E metal ligand. The *Zm*GLXI structure shows that there are no nearby residues in site B whose side chain could compensate for the absence of the E278 residue. Nevertheless, the second cavity retains the arginine residues involved in binding of glutathione conjugates [23], suggesting that *Zm*GLXI activity could be modulated by glutathione adducts in a yet to be disclosed allosteric regulatory mechanism.

In this work, we interrogate the number and location of *Zm*GLXI active sites through a combination of kinetic, spectroscopic, and crystallographic studies of two *Zm*GLXI variants obtained through site-directed mutagenesis. E144Q variant abolishes the negative charge of E144 metal ligand in site A, impairing its role in the catalytic mechanism; while V278E variant

introduces a negative charge in residue V278, aiming to restore the putative metal-binding ability of site B. Our results unambiguously assign the glyoxalase I activity to site A, whereas site B is shown to be devoid of glyoxalase I or II activities. In addition, our fluorescence quenching and crystallographic data shed light on the *Zm*GLXI reaction mechanism.

Results

Gene cloning, protein expression, and purification

In this work, *Zm*GLXI protein variants E144Q and V278E were cloned as described in the Methods, while the expression and purification was conducted according to our previously published protocol [23], followed by digestion to remove the hexa-histidine tags.

Catalytic activity of ZmGLXI, E144Q, and V278E proteins

Glyoxalase I activity measurements were conducted spectrophotometrically, by following the absorbance at 240 nm corresponding to the formation of SLG (Fig. 1). The V278E protein exhibited wild-type like activity in the presence of 100 μM Ni(II). However, the E144Q variant activity was not detectable in the same reaction conditions. Kinetic parameters for the wild-type and V278E protein were obtained assuming a Michaelis–Menten model, considering that the substrate HTA appeared through fast spontaneous reaction between MG and GSH with a Keq = 0.385 [33] (Fig. 2A). Unlike the behavior of glyoxalase I from *Plasmodium falciparum*, which showed biphasic kinetics [34], our enzymes present a linear trend, with Hill parameters of 0.95 (Fig. 2B,C). This is suggestive of the presence of only one catalytic active site per monomer, along with the absence of allosteric modulation from the putative second site, at least under the conditions tested. Kinetic parameters of both enzymes were in the same order of magnitude (Table 1).

Glyoxalase II activity assays

Previous reports indicate that the homodimeric *Pseudomonas aeruginosa* glyoxalase I GloA2 displays two distinct metal-binding sites: one active with Ni(II) and the other inactive with two Zn(II) ions, which exhibits a weak hydrolase activity [35]. Taking into account that glyoxalase II enzymes require a dinuclear Zn(II) center for activity, an attractive hypothesis would be that the same *Zm*GLXI protein displayed two active sites, respectively with glyoxalase I and glyoxalase II activities. This appears not to be the case for *Zm*GLXI, since a decay of SLG in the presence of

Table 1. Kinetic parameters of wild-type *Zm*GLXI and its V278E protein variant. Reaction medium was 50 mM MOPS buffer, pH 7.2, 100 μM Ni(II), at 25 °C

	wild-type *Zm*GLXI	V278E protein
V_{max} (IU/mg)	50.24 ± 1.40	33.86 ± 1.02
K_{mHTA} (μM)	80.91 ± 6.84	25.39 ± 3.11

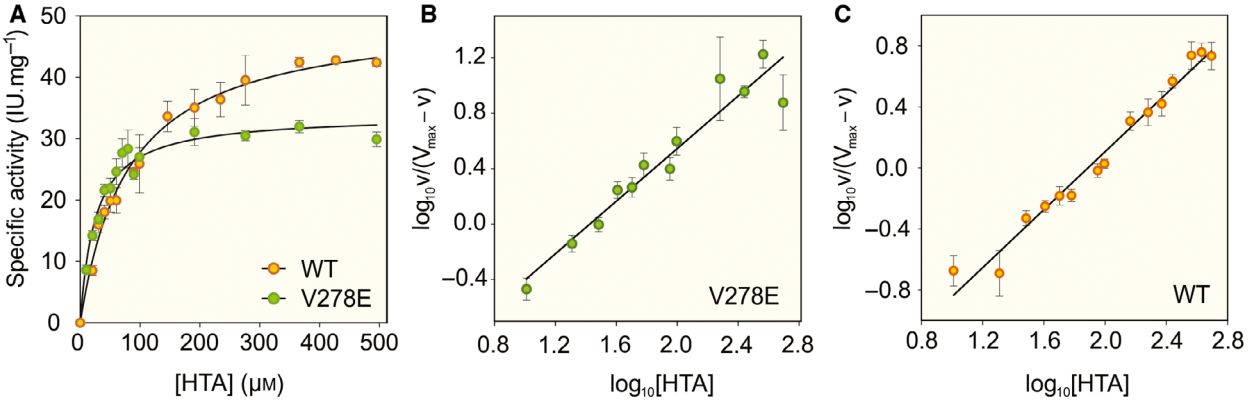

Fig. 2. Catalytic profile of *Zm*GLXI. (A) Typical Michaelis–Menten plots of wild-type *Zm*GLXI (*black circles*) and *Zm*GLXI-V278E enzymes (*white circles*) in the presence of 100 μM Ni(II). The hemithioacetal (HTA) resulting from spontaneous reaction between MG and GSH was considered as the substrate. The reaction medium was 50 mM MOPS buffer, pH 7.2. Hill plots of *Zm*GLXI-V278E protein (B) and *Zm*GLXI (C) resulted in Hill coefficients of 0.95. Error bars indicate standard deviations for three independent replicates.

wild-type *Zm*GLXI or its V278E variant, in a reaction medium supplemented with 100 μM Zn(II), could not be detected.

Electronic absorption spectra of Co(II)-substituted enzymes

Considering that Co(II) is the second preferred metal cofactor of *Zm*GLXI, accounting for 35% of the activity measured in the presence of Ni(II) [23], we obtained Co(II) bound surrogates of *Zm*GLXI and protein variants in order to probe their substrate-binding mode. High spin Co(II) displays electronic absorption bands in the visible spectral range that are sensitive to changes in the metal ion coordination sphere. In addition, binding of free thiols to Co(II) gives rise to strong ligand-to-metal charge-transfer bands around 340 nm; thus, binding of GSH should strongly affect the Co(II) environment. Spectra of wild-type *Zm*GLXI and its variants exhibited comparable spectroscopic features. The spectrum of Co(II)-*Zm*GLXI shows a broad band centered at 540 nm, typical of Co(II) with coordination number of 6, in an octahedral geometry (Fig. 3). Such coordination mode has been witnessed for Zn(II) and Ni(II) in homodimeric glyoxalases I [36–38]. However, the addition of GSH to Co(II)-*Zm*GLXI resulted in no spectral changes in the UV-visible region, suggesting that GSH binding to Co(II)-*Zm*GLXI leaves the free thiol beyond the coordination distance to the metal ion, without altering its coordination number or geometry.

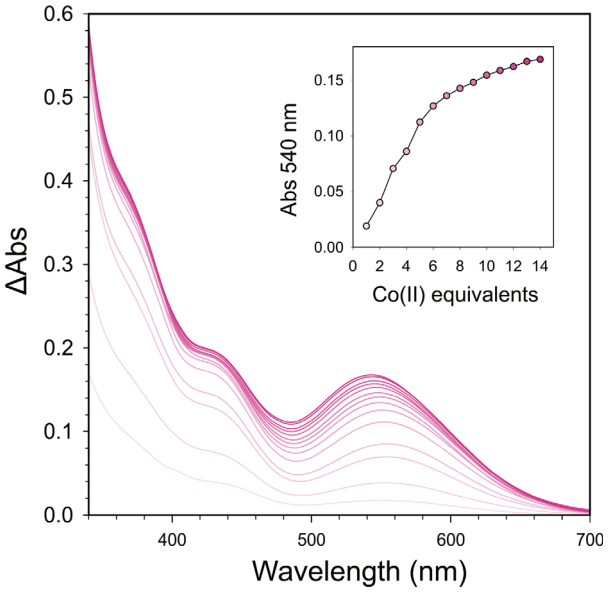

Fig. 3. Titration of apo *Zm*GLXI with Co(II) and GSH. A 1 mM solution of apoprotein in 50 mM Tris-HCl pH 7.2, 0.2 M NaCl was titrated with Co(II) (up to 14 equivalents) and then GSH (up to 4 equivalents). These procedures resulted in minor spectral changes in the visible spectral range, around 540 nm (*inset*).

Crystal structure of Co(II)-substituted ZmGLXI-E144Q and -V278E proteins

We crystallized Co(II)-substituted *Zm*GLXI variant proteins E144Q and V278E in a medium with GSH and MG, aiming to get insights into their kinetic behavior and localize the ligand binding sites. Two crystal forms appeared in the same crystallization conditions: Co(II)-E144Q and Co(II)-V278E *Zm*GLXI variants co-crystallized with GSH in tetragonal crystals (space group $P4_12_12$), whereas apo Co(II)-V278E rendered hexagonal crystals (space group $P6_3$), resembling the scenario witnessed for the histidine-tagged wild-type enzyme [23]. No MG molecules or its GSH adducts were found, suggesting that such species display low affinity for the protein in the abovementioned crystallization conditions. Crystals diffracted to high resolution, with the corresponding structures refined to 1.45 Å (tetragonal E144Q), 1.55 Å (tetragonal V278E), and 1.80 Å (hexagonal V278E). Both crystal forms harbor a single polypeptide chain per asymmetric unit, with intense density peaks for Co(II) ions in the corresponding site A metal-binding sites. Residues clearly defined in the electron density include amino acids 14–290 (tetragonal E144Q), 9–290 (tetragonal V278E), and 10–290 (hexagonal V278E). X-ray diffraction data collection and refinement statistics are summarized in Table 2.

Protein E144Q evaluates the effect of replacing a negatively charged carboxylate group by a neutral carboxamide group in residue 144, a metal ligand. The crystallographic structure of this protein shows that Gln144 side chain coordinates Co(II) ion through its carboxamide oxygen, leaving the amino group available for coordination of solvent and ligand molecules in the active site cavity (Fig. 4A). Since this protein is inactive, E144 probably catalyzes a proton transfer step, which cannot be replaced by a Gln144 residue, whose carboxamide amino group has a much higher pKa value than the native carboxylate group. This observation is in line with the reaction mechanism proposed by Cameron *et al.*, where E172 (the equivalent of E144 in human glyoxalase I) catalyzes the key proton migration step where HTA isomerizes into SLG [39].

As expected, V278E *Zm*GLXI variant showed a wild-type like, Co(II)-bound surrogate of site A (Fig. 4B). However, no electron densities compatible

Table 2. X-ray diffraction data collection and refinement statistics

	*Zm*GLXI-E144Q *tetragonal*	*Zm*GLXI-V278E *tetragonal*	*Zm*GLXI-V278E *hexagonal*
PDB entry	6BNZ	6BNN	6BNX
Data collection			
Space group	$P4_12_12$	$P4_12_12$	$P6_3$
Wavelength (Å)	0.9801	0.9800	0.9801
Number of frames	1800	1800	1800
Oscillation step (deg)	0.1	0.1	0.1
Detector distance (mm)	126.97	134.28	162.48
Exposure per frame (s)	0.025	0.025	0.025
Indexing and scaling			
Cell parameters *a, b, c* (Å)	69.89, 69.89, 119.7	69.95, 69.95, 119.4	82.11, 82.11, 74.97
α, β, γ (deg)	90, 90, 90	90, 90, 90	90, 90, 120
Resolution limit (Å)	1.45	1.55	1.80
No. of total reflections	689912	566347	274184
No. of unique reflections	53199	43782	26692
Average multiplicity[a]	13.0 (13.3)	12.9 (13.2)	10.3 (10.3)
$<I/\sigma(I)>$	18.5 (1.2)	19.3 (1.4)	19.7 (1.4)
R_{meas}	0.068(1.457)	0.068 (1.274)	0.067 (1.375)
CC (1/2)	0.999 (0.731)	0.999 (0.684)	1.000 (0.666)
Completeness (%)	99.7 (98.9)	99.8 (98.8)	99.9 (99.5)
No. chains per ASU	1	1	1
Solvent content (%)	45	45	45
Refinement			
Resolution range (Å)	45.68–1.45	45.70–1.55	41.05–1.80
No. of protein atoms	2211	2237	2228
No. of ligand atoms	35	26	1
No. of water molecules	228	223	195
R_{work}	0.199	0.188	0.181
R_{free}	0.231	0.231	0.221
RMS deviations			
Bond lengths (Å)	0.018	0.017	0.014
Bond angles (deg)	1.9	1.8	1.6
B-factor (average, Å^2)	27	29	38
MolProbity validation			
Clashscore	2.01	3.11	1.80
MolProbity score	1.55	1.40	1.51
Ramachandran plot			
Favored (%)	96.0	95.7	95.4
Allowed (%)	3.6	4.3	3.9
Disallowed (%)	0.4	–	0.7

[a] Values in parentheses correspond to the highest resolution shells (1.45–1.54, 1.55–1.64, and 1.80–1.91 Å, respectively).

with a transition metal ion were found near residue E278 in site B. This was rather unexpected, considering the remarkable similarity between sites A and B metal ligand residue positions. A structural α-carbon superposition of sites A and B of V278E protein allowed us to hypothesize that the main reason for the absence of Co(II) in site B is the presence of Val29 side chain, which would clash with residues E78 and Q226 if they coordinated a Co(II) ion (Fig. 4C).

The GSH binding site comprises residues R120, R161, and N212, which make specific H bond contacts with GSH; along with Y191, which provides hydrophobic interactions with the GSH glycyl moiety (Fig. 5). The GSH thiol group sits at 5.4 Å from Co (II) ion, leaving room for the MG moiety entrance upon displacement of water molecules W1 and W2. On the other hand, GSH appears bound to tetragonal crystals only, suggesting that the observed hexagonal ($P6_3$) *vs.* tetragonal ($P4_12_12$) space group switch is a consequence of GSH binding. By comparing the structures of V278E in tetragonal GSH-bound form with the hexagonal apo form, a conformational change can be witnessed. Upon GSH binding, the N- and C-terminal domains rotate about five degrees relative to one

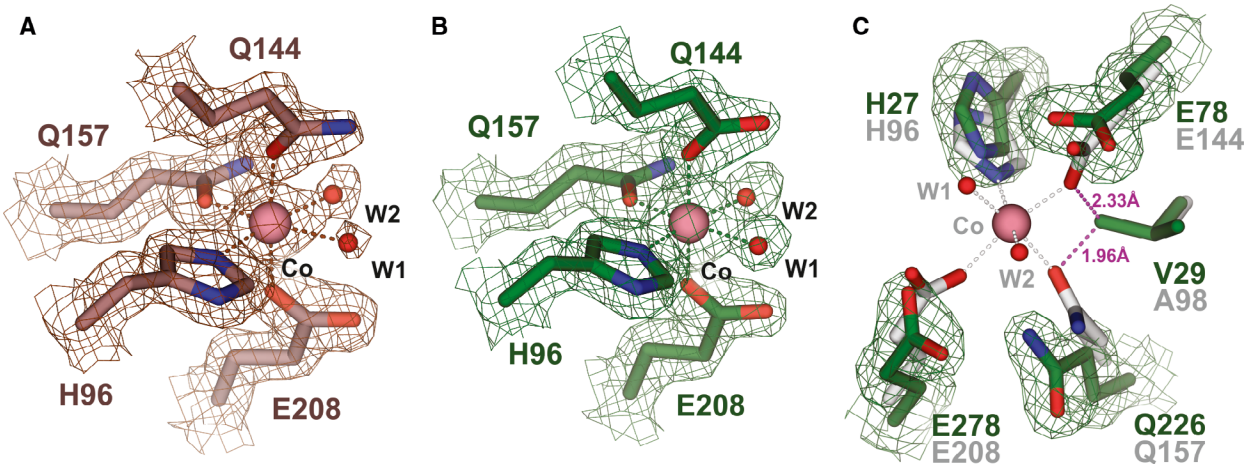

Fig. 4. Metal-binding site structure of: (A) E144Q variant site A (*brown*), (B) V278E variant site A (*green*). (C) Superposition of sites A and B of the V278E protein (*green* and *gray*, respectively). Dotted lines in *magenta* indicate clashing distances between V29, E78, and Q226. Metal coordination and H bonds are indicated as dotted lines. Water molecules W1 and W2 coordinating the Co(II) ion (*pink*) are indicated as *red* spheres. Residues E/Q144 and E208 define a vertical axis perpendicular to an equatorial square plane, comprising residues N157, H96, and water molecules W1 and W2.

another around the central hinge region, closing the substrate-binding site (Fig. 6A). The concurrent changes in interface-buried surface areas were calculated with the EPPIC server [40] in order to determine the regions involved in intermolecular interactions (Table 3). The minimal assemblies in the hexagonal $P6_3$ space group are pseudo-trimers, stabilized by hydrophobic interactions among residues I39, L50, E44, T43, and K53 in one chain, with residues T283, N232, L286, K287, N282, and S22 on the other; centered around helices α2 and α5, respectively. Due to the conformational change caused by GSH binding, these regions become separated and unable to interact, thereby disrupting the pseudo-trimers and the hexagonal crystal lattice (Fig. 6B). The GSH-bound protein assemblies comprise pseudo-dimers crystallizing in tetragonal $P4_12_12$ space group. In general, the tetragonal crystal lattice exhibited a higher buried surface area, which makes it more stable than the hexagonal one. This is consistent with the overall better diffraction quality of tetragonal *vs.* hexagonal crystals (*cf.* Table 2).

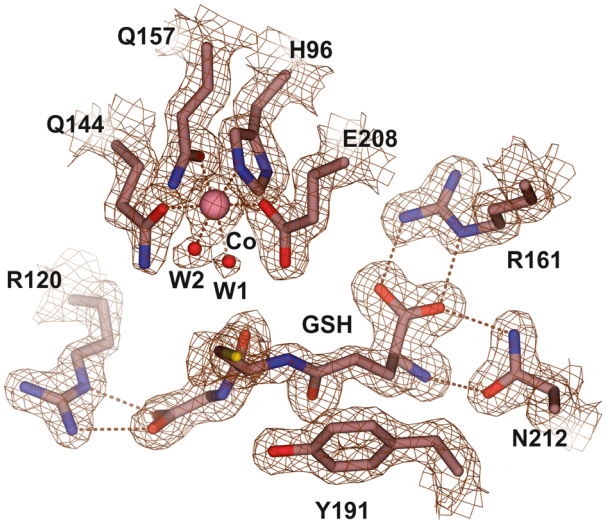

Fig. 5. Glutathione binding site of mutant E144Q. Dotted lines indicate metal coordination and H bonds. Water molecules W1 and W2 coordinating the Co(II) ion (*pink*) are indicated as *red* spheres.

The conformational change after GSH binding generates a tunnel in the enzyme active site, which was analyzed with CAVER 3.0.1 [59]. As shown in Fig. 7, GSH closes one end of the tunnel, leaving a narrow tunnel that may only allow the entrance of water molecules. The other end remains open and accessible to small ligands up to 3–4 Å, such as solvent molecules and MG. The trajectories calculated indicate that the metal cofactor is accessible to a MG molecule entering through the open side of the tunnel, the MG entrance side. Thus, modeling of MG bound by displacement of W1 and W2 water molecules, near the tunnel bottleneck, is compatible with a reaction mechanism where (*S*)-HTA is generated stereospecifically in the active site, but not the (*R*)-HTA diastereomer (Fig. 8). A similar binding mode was determined for the strong inhibitor HIPC (S-(*N*-hydroxy-*N*-*p*-iodophenylcarbamoyl) glutathione) by Cameron *et al.* [41].

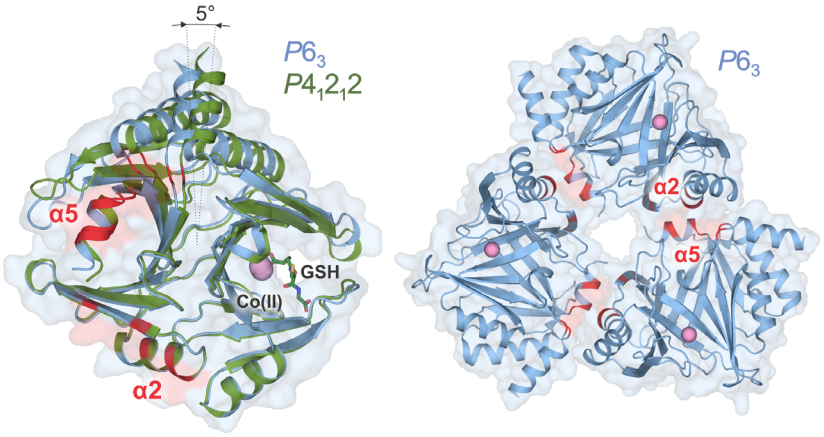

Fig. 6. Comparison of tetragonal ($P4_12_12$, *green*) and hexagonal ($P6_3$, *blue*) forms of the V278E variant, disclosing the conformational change taking place upon GSH binding (*left*), and the pseudo-trimer structure (*right*), highlighting the interaction areas disrupted by the conformational change; specifically, areas centered on helices α2 and α5 (*red*).

Fluorescence quenching analysis

The generally accepted reaction mechanism of glyoxalase I involves a single substrate, which is the HTA racemate formed through spontaneous reaction of GSH and MG (Fig. 1) [33,39,42]. However, our crystallographic data show that *Zm*GLXI is able to bind intact GSH in the active site, giving rise to a tunnel with independent binding sites for GSH and MG (Fig. 7). Therefore, the GSH-bound enzyme could also bind MG and catalyze the formation of (*S*)-HTA, instead of having to exchange GSH with (*S*)-HTA from the surrounding medium. In other words, our crystallographic data indicate that GSH does not competitively inhibit the enzyme, under the assumption that the HTA racemate is the true substrate. This observation prompted us to postulate a reaction mechanism based on HTA generation *in situ* upon MG binding to the GSH-enzyme complex. We decided to explore this possibility by following the quenching of intrinsic fluorescence upon ligand binding. *Zm*GLXI contains two tryptophan residues, W17 and W275, located at about 30 and 15 Å from the active site metal ion, respectively. Both residues donate an H bond to specific motifs in the protein, namely, W17-$N^{\varepsilon 1}H\cdots O^{\gamma}H$-S237 and W275-$N^{\varepsilon 1}H\cdots$O-R161. W275 lies in a rigid, more hydrophobic pocket, with an average B-factor of 27 $Å^2$, significantly lower than the 43 $Å^2$ of W17. Thus, W275 is expected to significantly contribute to the intrinsic *Zm*GLXI fluorescence, while probing the active site due to its proximity to the metal ion.

All three native ligands were shown to decrease the intrinsic *Zm*GLXI tryptophan fluorescence, evidenced as reduction in emission intensity at 341 nm after excitation at 295 nm. Two binding scenarios were tested. First, the titration order was: Co(II), GSH, and MG; and second: Co(II), MG, and GSH. Next, Stern–Volmer plots were calculated for each of the six titration curves (Fig. 9), allowing us to obtain apparent quenching constants (K_{SV}) for each process (Table 4). Co(II) exhibited a quenching constant of 12.5 μM for the metal-free protein (*titration 1*), while MG and GSH exhibited quenching constants of K_{MG} = 2.73 μM and K_{GSH} = 8.85 μM, for quenching of the Co(II)-bound protein intrinsic fluorescence (*titration 2*). Then, both constants decrease approximately four-fold in *titration 3*: the K_{SV} constant of MG in the presence of GSH ($K_{MG/GSH}$) is 0.637 μM, whereas that of GSH in the presence of MG ($K_{GSH/MG}$) is 2.89 μM. In other words, the apparent affinity of each substrate is higher in the presence of the other. Bearing in mind our crystallographic data, which show that the protein forms a stable complex with GSH, the values of K_{GSH} and $K_{MG/GSH}$ can be attributed to static quenching processes, that is binding of GSH to the cobalt enzyme, and binding of MG to the cobalt enzyme-GSH complex. In contrast, quenching by MG alone is likely to occur through a collisional process, since the protein does not exhibit a clear MG binding site in the absence of GSH. Finally, the quenching mechanism of GSH in the presence of excess free MG and the cobalt enzyme is likely obscured by the formation of HTA in solution, with a complex mixture of HTA, GSH and MG interacting with the protein through collisional and static processes. Nevertheless, since $K_{GSH/MG}$ and $K_{MG/GSH}$ are significantly different, these quenching processes cannot be explained as a mere result of quenching by the HTA formed in solution; otherwise, $K_{GSH/MG}$ and $K_{MG/GSH}$ would be similar. Instead, the metalloenzyme seems to interact differently with either substrate, preferentially binding GSH and then MG.

Discussion

As previously reported by us [23], the maize glyoxalase I is a Ni(II)-dependent monomeric metalloenzyme. From the crystallographic structure, we determined the

Table 3. Amino acid residues involved in intermolecular interactions stabilizing mutants E144Q and V278E crystal forms, compared with wild-type *Zm*GLXI, as obtained with the EPPIC server (www.eppic-web.org). Amino acid residues are sorted by decreasing value of buried surface area (BSA), expressed as percent relative to the total accessible surface area (indicated between parentheses), for each interface of interacting chains A and B (defined arbitrarily). Only residues with relative BSA > 50% are shown. Major assemblies comprise the largest BSA values, respectively, dimers for tetragonal $P4_12_12$ space group and trimers for hexagonal $P6_3$ space groups

	Tetragonal E144Q	Tetragonal V278E	Hexagonal V278E	Hexagonal WT
PDB code (space group)	6BNZ ($P4_12_12$)	6BNN ($P4_12_12$)	6BNX ($P6_3$)	5D7Z ($P6_3$)
A. Interface Area (Å^2)	817	853	544	351
Chain A	L289 (91)	L289 (94)	I39 (100)	L253 (97)
	D281 (86)	T283 (85)	L50 (92)	R254 (79)
	T283 (84)	D281 (84)	E44 (66)	Q255 (54)
	P70 (84)	P70 (84)	T43 (56)	
	K49 (82)	K49 (81)	K53 (51)	
	P152 (77)	P152 (77)		
	N72 (70)	L286 (71)		
	L286 (69)	N72 (70)		
	M48 (61)	H290 (56)		
	K287 (51)	K287 (54)		
	H290 (50)	E71 (52)		
		H290 (51)		
Chain B	V215 (99)	V215 (100)	T283 (94)	V131 (98)
	T92 (90)	T92 (91)	N232 (80)	Y105 (74)
	I90 (76)	K117 (77)	L286 (76)	Q147 (65)
	K117 (73)	I90 (77)	K287 (62)	E109 (60)
	G91 (68)	I118 (75)	N282 (58)	D103 (60)
	N136 (64)	Q136 (69)	S22 (54)	S129 (58)
	I118 (61)	G91 (66)		
	N212 (61)	N212 (62)		
	K190 (57)	K190 (60)		
		Y218 (55)		
B. Interface Area (Å^2)	468	488	338	209
Chain A	K183 (96)	K183 (96)	V131 (86)	H295 (67)
	L180 (87)	L180 (87)	Y105 (75)	H294 (50)
	L181 (70)	L181 (70)	E109 (61)	
	D185 (57)	D185 (57)	S129 (61)	
			D103 (58)	
			Q147 (56)	
Chain B	K183 (96)	K183 (96)	L253 (98)	H290 (70)
	L180 (87)	L180 (87)	R254 (78)	K287 (62)
	L181 (70)	L181 (70)	Q255 (53)	
	D185 (57)	D185 (57)		
C. Interface Area (Å^2)	322	330	216	200
Chain A	Y235 (89)	Y235 (89)	L180 (84)	L180 (84)
	P258 (88)	P258 (85)	I169 (82)	I169 (70)
	G257 (87)	G257 (85)	K183 (55)	
		N263 (53)		
Chain B	S113 (83)	S113 (84)	G84 (93)	G84 (88)
	E109 (58)	E109 (71)	K60 (66)	K60 (57)
	K106 (51)		V85 (54)	V85 (50)
D. Interface Area (Å^2)	238	240	122	0
Chain A	T245 (78)	T245 (76)	-	N.A.
	G249 (54)	G249 (58)		
	G250 (54)	K246 (52)		
		K251 (51)		
Chain B	Y83 (83)	Y83 (75)	-	N. A.
	G84 (68)	G84 (68)		
	K60 (63)	K60 (63)		
		Y81 (61)		
BSA (Å^2)	1845	1911	1220	

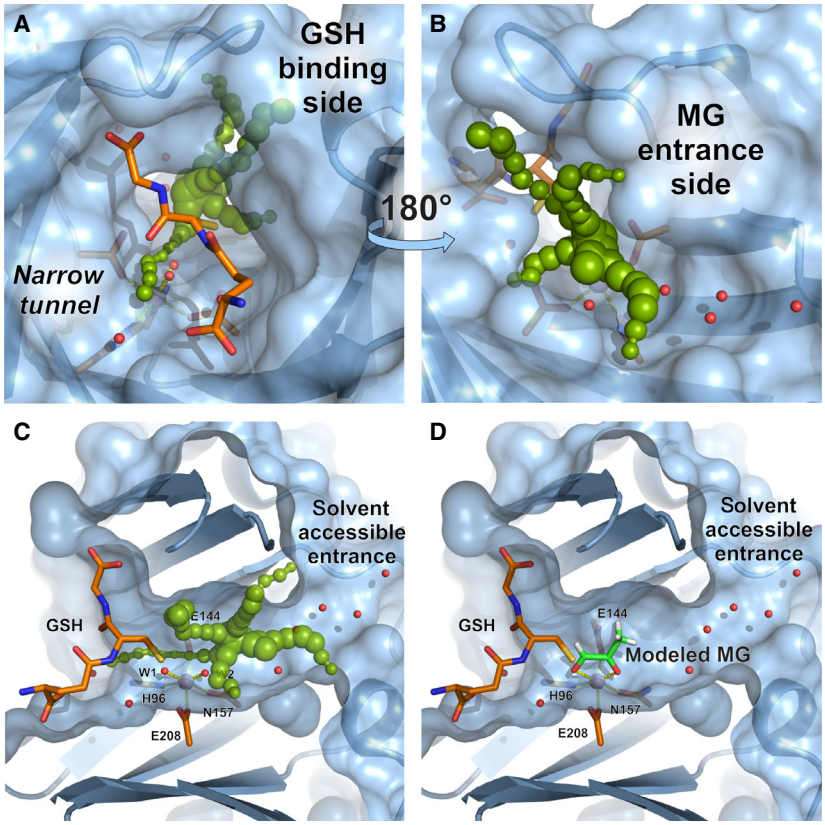

Fig. 7. Structure of GSH-bound *Zm*GLXI active site, as determined in the V278E protein structure (PDB 6BNN). The conformational change after GSH binding turns the active site into a closed tunnel, which was analyzed with CAVER 3.0.1 [59]. This program calculates the shape and size of voids and channels inside macromolecules by filling them with spherical probes of maximal size and connecting their centers to provide trajectories. In this way, the obtained system of connected spheres, or Voronoi diagram, represents the tunnel shape and size. In the case of the GSH-bound *Zm*GLXI active site, the set of *green* spheres (scaled down 3X for the sake of figure clarity) in panels A, B, and C indicates the size and possible trajectories of molecules accessing the active site. (A) GSH closes one end of the tunnel (the GSH binding side), leaving a narrow channel that may only allow entrance of water molecules. (B) The other end of the tunnel remains open and accessible to small ligands up to 3–4 Å, such as solvent molecules and MG (the MG entrance side). (C) A bottleneck is formed near the W2 molecule, between the narrow channel beneath the GSH molecule and the solvent-accessible MG entrance. (D) This bottleneck represents the farthest site that MG can reach before binding to the metal ion by displacement of water molecules W1 and W2.

presence of two cavities, with only one of them exhibiting the metal-binding tetrad conserved in the active sites of glyoxalase I enzymes (site A: H96/E144/Q157/E208). However, in the second cavity, *Zm*GLXI harbors a valine residue (V278) in place of the conserved E208 residue (site B: H27/E78/Q226/V278). In an attempt to test the functionality of each cavity, we generated two enzyme variants (named E144Q and V278E) and analyzed their biochemical, biophysical, and structural characteristics. The E144Q change in site A has been previously studied, considering that E172 of human glyoxalase I (the surrogate of *Zm*GLXI E144) had been proposed as a general base in the reaction mechanism [43]. In agreement with previous results, we found that E144Q protein is inactive, but most importantly, the *Zm*GLXI site B is also devoid of glyoxalase I activity. The presence of V278 disrupting the conserved metal-binding tetrad may have resulted in the loss of site B glyoxalase I activity. Nevertheless, the V278E mutation did not restore Co(II) binding at site B, indicating that additional mutations are needed to recover this metal-binding site as well as its putative ancient activity.

Mature Co(II)-substituted protein variants and the wild-type enzyme exhibited weak electronic absorption bands in the visible region, suggestive of bound Co(II) ions in hexa-coordinated octahedral sites. By titration of apoenzymes with Co(II), we found that several molar equivalents were needed to reach maximal absorption at 540 nm, suggesting that the folded apoprotein has low affinity for the metal cofactor. This observation concurs with our previous results with the

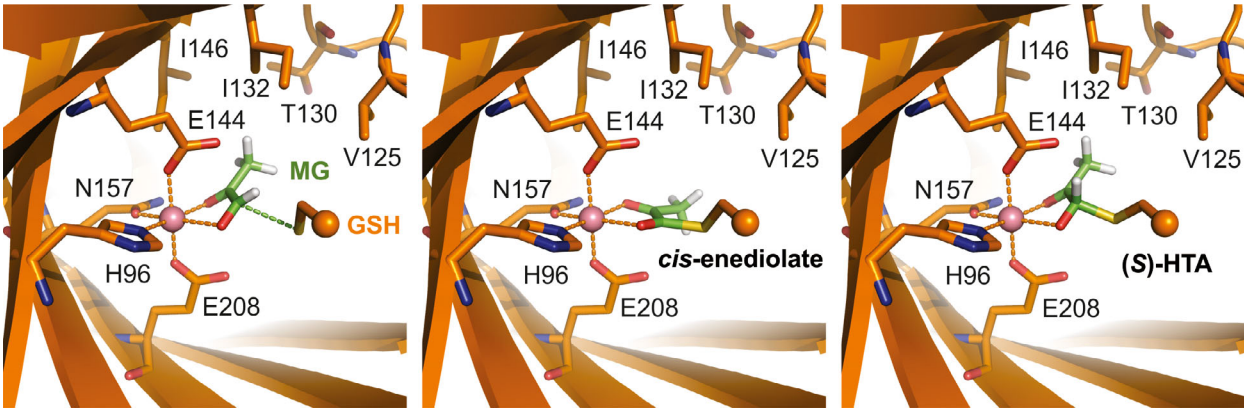

Fig. 8. Model of MG binding to the *Zm*GLXI-GSH complex. The ligand (*green*) was manually placed in the structure of mutant V278E (which has a wild-type like active site), assuming that it displaces water molecules W1 and W2, adopting a *cis* conformation and orienting the methyl moiety toward a hydrophobic patch comprising residues I146, I132, T130, and V125. In this way, the electrophilic attack by GSH (simplified as the *orange* sphere) can only take place from the E208 side (*left*), which leads to the *cis*-enediolate (*middle*), and then the (*S*)-HTA diastereomer by protonation of from the E144 side (*right*).

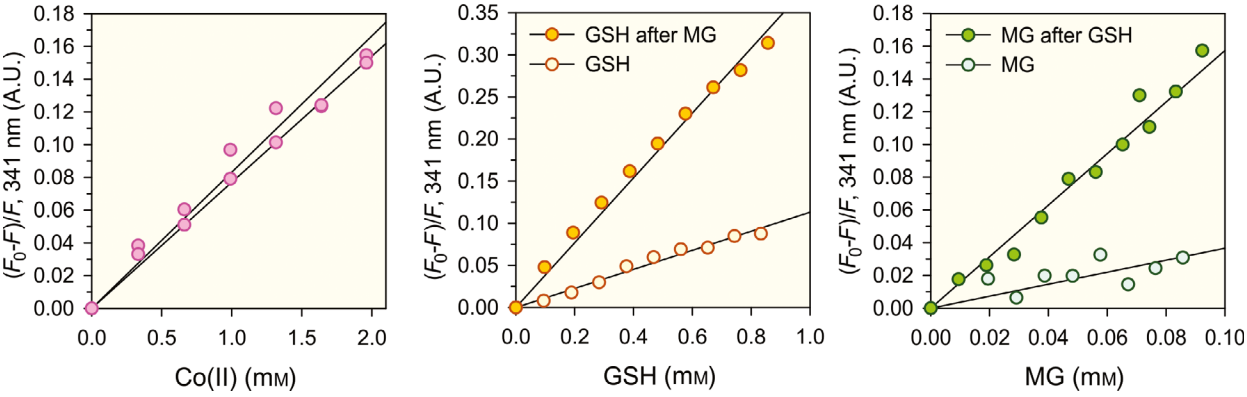

Fig. 9. Stern–Volmer plots for quenching of wild-type *Zm*GLXI intrinsic fluorescence titrated with Co(II), GSH and MG. *Black* circles indicate titrations with Co(II), GSH, or MG only, whereas *red* circles indicate titrations with GSH and MG in the presence of MG and GSH, respectively. The protein concentration was 5 μM in a medium consisting of 50 mM Tris-HCl, pH 7.2, 0.2 M NaCl. Titrations were performed in the concentration ranges 0–2 mM for Co(II), 0–1 mM for GSH, and 0–0.1 mM for MG. The corresponding K_{SV} constants are listed in Table 3.

Ni(II) surrogate [23]. Further addition of GSH to Co (II)-saturated enzymes did not result in extra spectral features, indicating that the thiol of bound GSH remains far from Co(II) ion; otherwise a characteristically intense charge-transfer absorption band around 340 nm would have been witnessed. The fact that all protein samples exhibited comparable electronic spectra suggests that they share similar Co(II) binding sites; that is, the E144Q protein would still be able to bind Co(II), whereas V278E would keep only one metal equivalent. Overall, these results were not sufficient to discern the structural features of each variant, so we decided to solve their crystallographic structures in the presence of Co(II), GSH, and MG, in order to shed light on their substrate-binding modes.

Both variants crystallized in the same conditions as wild-type *Zm*GLXI, but remarkably switched to a different space group due to a conformational change induced by GSH. We obtained high-resolution structures that allowed us to confirm the presence of Co(II) ions in site A of both proteins, as well as its absence in their corresponding sites B, in agreement with the spectroscopic data. Besides, the active sites of both protein variants exhibit a closed conformation in their GSH-bound form, giving rise to a tunnel-shaped cavity with two defined ends, holding the metal-binding site

Table 4. Stern–Volmer constants for intrinsic fluorescence quenching assays. Titrations correspond to: (1) apoenzyme with Co (II), (2) Co(II)-*Zm*GLXI with GSH or MG, and 3) Co(II)-*Zm*GLXI with GSH or MG, in the presence of MG or GSH, respectively. See Fig. 9

Ligand added	Stern–Volmer constants (μM)		
	Titration 1	Titration 2	Titration 3
Co(II)	12.5 ± 0.72	–	–
GSH	–	K_{GSH} = 8.85 ± 0.46	$K_{GSH/MG}$ = 2.89 ± 0.11
MG	–	K_{MG} = 2.73 ± 0.65	$K_{MG/GSH}$ = 0.637 ± 0.028

in the middle. One end is occupied by the GSH ligand, whose thiol moiety remains at 5.4 Å from Co(II) ion, near the tunnel bottleneck. The other end becomes a solvent-accessible cavity that allows small molecules like water and MG to reach the metal coordination shell. In fact, our fluorescence quenching assays confirmed that MG preferentially binds to the GSH-enzyme complex instead of the free enzyme. These results prompted us to postulate a reaction mechanism where GSH and MG react in the enzyme active site, given that binding of GSH does not competitively inhibit the binding of MG. On the contrary, the enzyme seems able to accommodate both substrates in a catalytically favorable orientation (Fig. 7D), without requiring them to leave the active site to react in solution and return to complete the isomerization reaction.

Based on the established reaction mechanisms of HTA formation in solution and its isomerization into SLG, a mechanism can be postulated for the two-substrate case (Fig. 10). The formation of HTA starts with the GSH thiol nucleophilic attack on C1 of the MG aldehyde group, developing a positive charge on the thiol and a negative charge on the C1 oxygen atom. If Co(II) ion is assumed to stabilize such additional negative charge, one of the glutamate residues is expected to detach from the metal ion, being E144 a good candidate, which is ideally positioned to deprotonate the C1 aldehyde group, giving rise to a dibasic *cis*-enediolate. Correspondingly, if Co (II) ion is assumed to stabilize the two enediolate negative charges, this time E208 would detach from the metal ion (since E144 is already protonated), favorably located to deprotonate the positively charged thiol group. Next, E144 necessarily should mediate the enediolate protonation at C2, since the reaction is stereospecific for S-D-lactoyl (and not L-lactoyl) glutathione. A second protonation releases the SLG product, returning the enzyme to its resting state. This step is probably assisted by E208, which needs to lose a proton in order to bind the metal cofactor. Finally, it is worth mentioning that, while the glutamate residues are good candidates to perform both deprotonation steps, the product release protonations might involve water molecules, which are free to enter the active site through either side of the tunnel. Further kinetic and spectroscopic assays may help to clarify whether the reaction mechanism is sequential ordered or random. Techniques like UV-Vis spectroscopy and time-correlated single photon counting for fluorescence lifetime measurements, coupled to photodiode-array stopped-flow instruments, will likely shed light on the sequence of events during catalysis, taking advantage of the presence of only two tryptophan residues asymmetrically located around the active site, and the fact that the enzyme is fully active in its Co(II)-substituted form.

In this report, we confirmed that *Zm*GLXI conserves only one catalytic site (site A) for MG detoxification, a feature witnessed for a number of glyoxalases from plants. We also show that site B is devoid of glyoxalase I or II activities, although a putative regulatory function for this site remains to be determined [34,44]. On the other hand, closing of site A upon GSH binding provides a noticeable example of a protein crystallization space group switch driven by a conformational change. Since the closed active site becomes a tunnel-shaped cavity with independent binding sites for GSH and MG, we postulated a two-substrate model for GLXI, as recently proposed by Lages *et al*. for yeast GLXI, based on elaborate data processing algorithms [45]. Our model provides a plausible mechanism for generation and isomerization of (*S*)-HTA into SLG in the active site, starting from bound GSH and MG. However, this does not preclude the enzyme from catalyzing the HTA racemate isomerization into SLG. Indeed, Landro *et al*. [46] showed that yeast glyoxalase I exhibits lower substrate selectivity, being active against two chemically synthesized glutathiolactaldehyde isomers, in lieu of the unstable HTA. Since free GSH might be in short supply under harsh oxidative or temperature stress conditions, the HTA racemate might become a major glyoxalase I substrate, driving the evolution of glyoxalases with extended substrate specificity.

Materials and methods

General

Methylglyoxal (MG) and glutathione (GSH) were purchased from Sigma-Aldrich (St. Louis, MO, USA). All chromatographic steps were performed on an Amersham Biosciences liquid chromatography system operating at 4 °C. Metal standards were purchased from Fisher Scientific and were diluted with ultrapure water. All other chemicals used in this study were commercially available and were of the highest quality.

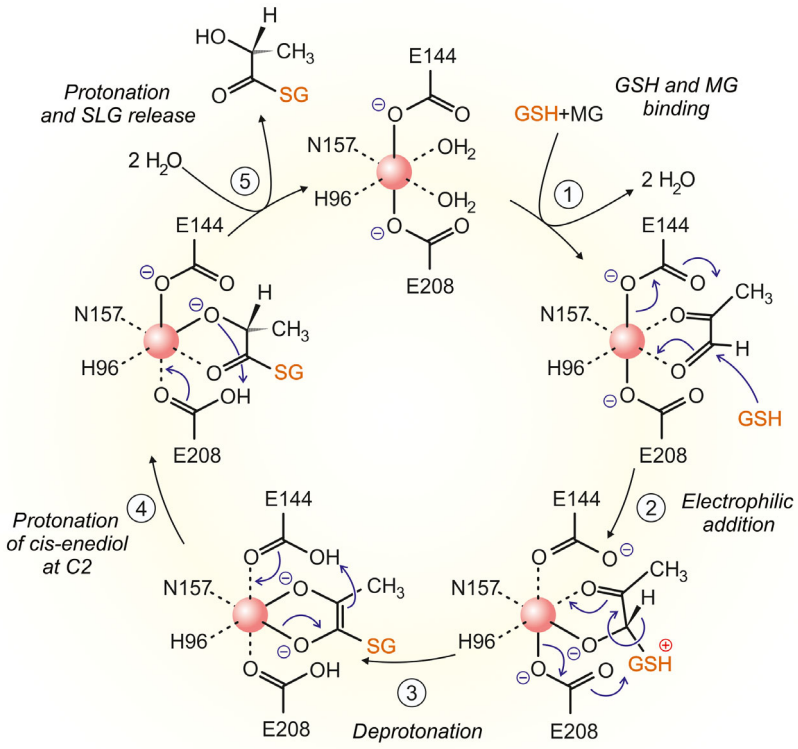

Fig. 10. Proposed reaction mechanism where *Zm*GLXI catalyzes both the formation of (*S*)-HTA and its isomerization into SLG. In the resting state both E144 and E208 would be deprotonated, providing two negative charges to balance the divalent Co(II) cofactor, which presents two available coordination positions occupied by water molecules W1 and W2. Reaction steps are: (1) MG binding to a cleft between E144 and the GSH thiol moiety, through displacement of water molecules W1 and W2 (*cf.* Fig. 8); (2) electrophilic addition reaction of GSH from the E208 side to render the (*S*)-HTA, where a positive charge develops in the GSH thiol moiety; (3) deprotonation of (*S*)-HTA at C1 by E144 to produce a *cis*-enediolate, stabilized by direct coordination to the metal cofactor; (4) protonation of the *cis*-enediolate at C2 by E144, rendering SLG; and (5) protonation and release of SLG.

Gene amplification and cloning

The coding DNA sequence of *Zea mays* glyoxalase I (Zm00001d024245) and two site specifics mutants were cloned into a pET28b(+) expression vector (Novagen), between *Nhe*I and *Xho*I restriction sites. This cloning strategy resulted in the addition of a cleavable His-Tag sequence at the N-terminus of each protein product. The primer sequences are depicted in Table 5.

For the generation of V278E variant, we used the Megaprimer method [47], using primers GlxI-Fw and megaprimer V278-Rv containing the mutation of interest. PCRs were developed in a final volume of 25 μL, 0.2 mM deoxyribonucleotide triphosphates (dNTPs), 1 μM oligonucleotide primers, 1 X amplification buffer, and 0.02 U/μL of Phusion DNA Polymerase (Thermo Fisher). The amplification was performed in a Gene Amp PCR System 2400 thermocycler (Perkin Elmer), starting with a 30-s stage at 98 °C, followed by 25 cycles comprising three steps: 5 s at 98 °C, 20 s at 60 °C, and 20 s at 72 °C; plus a final 5 min stage at 72 °C.

Construction of variant E144Q was previously done by the Overlap Extension PCR method [23]. In a first stage, two fragments of glyoxalase I were amplified. Primers GlxI-Fw and E144Q-Rv were used to amplify a fragment of 445 bp (PCR 1), whereas primers GlxI-Rv and E144Q-Fw were used for extension of a 462 bp fragment (PCR 2). Next, a step of synthesis of strands complementary to the single strand DNA generated by the overlapping of

Table 5. Primer sequences. Cleavage sites for the restriction enzymes *Nhe*I and *Xho*I appears underlined. In bold are shown the replaced codon for glutamine or glutamic acid residues

Primer	Sequence
GlxI-FW	ATCGCTAGCATGGCAACCGGTAGTG
GlxI-RV	AACCTCGAGTCAGTGGAGTTCCTTGAG
E144Q-FW	TACATGTTT**CAG**CTTATCCAGAGGG
E144Q-RV	CCCTCTGGATAAG**CTG**AAACATGTA
V278E-RV	ATCCTCGAGTCAGTGGAGTTCCTTGAGG AAGTCGGTGTTGTCAACCAGTTCCAC T**TTC**CAGCC

individually mutated fragments was performed, namely, the purified fragments obtained from PCR 1 and PCR 2. To this end, both reactions were developed in a final volume of 50 μL, 0.2 mM dNTPs, 1 X amplification buffer, and 0.02 U/μL DNA Phusion Polymerase. The PCR comprised a 30-s stage at 98 °C, followed by 10 cycles of: 5 s at 98 °C, 20 s at 60 °C, and 20 s at 72 °C; plus a final 5 min stage at 72 °C. Subsequently, 0.2 μM of the GlxI-Fw and GlxI-Rv primers were added and the last PCR was performed, comprising a 30-s stage at 98 °C, followed by 30 cycles of: 5 s at 98 °C, 20 s at 60 °C and 20 s at 72 °C; plus a final 5 min stage at 72 °C.

Protein production and purification

Wild-type *Zm*GLXI as well as variants V278E and E144Q were recombinantly produced in *Escherichia coli* BL21 Rosetta cells, using the previously mentioned constructs. This system yields high expression levels of each recombinant protein fused to an N-terminal hexa-histidine tag. In a typical protein preparation, 400 mL of transformed *E. coli* BL21 Rosetta culture were grown in auto-induction medium [48], supplemented with trace metal ions, and incubated for 24 h at 30 °C, as previously described [23]. Then, the bacterial cultures were harvested by centrifugation and suspended in 50 mM Tris-HCl pH 8.0, 1 mM phenylmethylsulfonyl fluoride, 0.01 mg/mL DNAse and 5 mM $MgCl_2$. Cells were lysed by six sonication pulses of 30 s, whereas cell debris was pelleted by ultracentrifugation at 12 000 ***g*** in an SS34 rotor of a Sorvall centrifuge. The bacterial lysate was applied onto a column of Ni-NTA (Invitrogen, Carlsbad, CA, USA). After washing with 50 mM Tris-HCl pH 8.0, 0.3 M NaCl, 20 mM imidazole, the fusion protein was eluted with 50 mM Tris-HCl pH 8.0, 300 mM NaCl, and 250 mM imidazole. Fractions of each protein were pooled and dialyzed against 50 mM Tris-HCl pH 7.2, 0.2 M NaCl. His-Tag removal was performed by incubating the protein sample with a 1 : 100 ratio of thrombin during 1 h at 37 °C in Tris-HCl pH 7.2, 0.2 M NaCl. Tag-free protein samples were obtained through an additional step with Ni-NTA IMAC, where the His-Tag and undigested protein were retained. Finally, the tag-free protein samples were concentrated using an Amicon centrifugal filter device. The enzyme concentration was determined spectrophotometrically by measuring the absorbance at 280 nm and using a theoretical extinction coefficient of $\Delta\varepsilon$ (280 nm) = 37 945 M^{-1} cm^{-1}. This parameter was calculated from the amino acid sequence by applying a modified Edelhoch method [49]. The Bradford colorimetric assay was also used to corroborate these measurements [50]. Protein purity was assessed by SDS/PAGE.

Preparation of Apoenzymes

Apoprotein samples used in electronic spectroscopy were prepared by two extensive dialysis step against > 100 volumes of 50 mM Tris-HCl pH 7.2, 0.2 M NaCl, 40 mM EDTA over a 12 h period under stirring. EDTA was removed from the resulting apoenzyme solution by three dialysis steps against > 100 volumes of 50 mM Tris-HCl pH 7.2, 1 M NaCl, and three dialysis steps against > 100 volumes of 50 mM Tris-HCl pH 7.2, 0.2 M NaCl. The last step consisted in two dilution/concentration cycles with 50 mM Tris-HCl pH 7.2, 0.2 M NaCl in an Amicon centrifugal filter to reach a final protein concentration of ~ 1 mM. All dialysis steps were performed at 4 °C.

Glyoxalase I activity

Kinetic parameters were determined measuring the initial rates of formation of S-D-lactoylglutathione at 240 nm, assuming a $\Delta\varepsilon$ (240 nm) = 3370 M^{-1} cm^{-1} [10]. The measurements were performed in a reaction medium consisting of 500 μL of 50 mM MOPS buffer, pH 7.2, 100 μM $NiCl_2$, at 25 °C, in a Jasco V-550 UV-vis spectrophotometer. The amount of enzyme ranged between 100 and 200 nM. The GSH concentration was kept constant at 1.7 mM, whereas the MG concentration was varied from 10 to 1000 μM. Measurements were conducted at least in triplicate. Kinetic constants were determined by fitting the initial rates data to the Michaelis–Menten equation, considering the hemithioacetal (HTA) formed spontaneously through a fast reaction of GSH and MG in solution, with an equilibrium constant Keq = 0.385 [33]. The HTA concentration was calculated by applying the identity: Keq = [HTA]/(([GSH] − [HTA]) ([MG] − [HTA])), where square brackets indicate concentrations at equilibrium of HTA, GSH, and MG, respectively. Hill coefficients were calculated from Hill plots, as the slopes of logarithmic plots of fractional activity against substrate concentration.

Glyoxalase II activity

The measurement of activity against SLG (Sigma) was performed in a medium composed of 100 mM MOPS pH 7.2, 100 μM $ZnSO_4$ at 30 °C [51]. SLG was used at a final concentration of 900 μM, previously dissolved in 100 mM MOPS at pH 7.2. The reaction was monitored at 240 nm and 25 °C 298 K in a Jasco V-550 UV-vis spectrophotometer.

Electronic spectroscopy of Co(II)-substituted derivatives

A solution of ~ 1 mM apoprotein in 50 mM Tris-HCl pH 7.2, 0.2 M NaCl, was titrated by stepwise addition of 0.1 equivalents of a $CoSO_4$ solution prepared in the same buffer. After each addition, a spectrum between 300 and 800 nm was recorded at room temperature in a UV-Vis Jasco V-550 spectrophotometer, in a 1 cm path length cuvette. Differential spectra were obtained by subtracting the spectrum of the apoprotein using the Spectra Manager

suite (Jasco Corporation, Hachioji, Japan) and plotted in SIGMA PLOT 12.0 (Systat Software, San Jose, CA, USA). The final Co(II)-titrated protein was then used for titration with GSH, following an analogous protocol. Finally, the resulting protein samples containing several fold molar excess of Co(II) (~ 14 mM) and GSH (~ 4 mM) were used for crystallization trials (see below).

Protein crystallization

*Zm*GLXI-V278E and *Zm*GLXI-E144Q crystals were obtained by varying precipitant and protein concentrations in VDX plates (Hampton Research) with a hanging-drop setup, using as starting point the crystallization condition determined for wild-type *Zm*GLXI (4.0 M sodium formate, 1% (w/v) PEG 4000, pH 9.7 [23]). Optimized crystallization drops consisted of 4.0 μL 1 : 1 mixtures of protein sample (25 mg/mL in 50 mM Tris-HCl pH 7.2, 0.2 M NaCl, 5 mM GSH) and reservoir solution, prepared with 0.5% (w/v) PEG 4000, 4.2 M sodium formate. Due to the toxic long-term effects of MG, crystals were soaked in 4.5 mM MG before flash freezing in liquid nitrogen and data collection. We obtained block crystals for Z*m*GLXI-E144Q, while oval and needle bunch morphologies were observed for the *Zm*GLXI-V278E. Crystals were appeared after 15 days of incubation at 20 °C. Samples were mounted in nylon loops (Hampton Research) and flash-cooled in liquid nitrogen, using 7 M sodium formate as cryoprotectant.

X-ray diffraction data collection, structure determination, and analysis

Diffraction data from *Zm*GLXI-V278E and *Zm*GLXI-E144Q crystals were collected at 100 K at the PROXIMA 2A beamline of the SOLEIL synchrotron (France), equipped with a Dectris EIGER 9M detector. Data were processed with XDS [52] using the graphical user interface XDSGUI. A total of 5% of the recorded reflections were flagged for cross-validation. Molecular replacement was carried out with PHASER [53] using the *Zm*GLXI structure as template (PDB 5D7Z) [23]. Refinement was performed with REFMAC5 [54] from the CCP4 Suite of Programs [55], and manual building was conducted with COOT [56]. Structure validation was performed with MOLPROBITY [57], the wwPDB Validation Service [58] and the built-in functions implemented in COOT. Details of data collection parameters and refinement statistics are shown in Table 2. Figures were prepared with PYMOL 1.8 (Schrödinger, New York, NY, USA) and CorelDraw X7 (Corel Corporation, Ottawa, Canada).

Fluorescence quenching assays

Intrinsic fluorescence excitation and emission spectra were obtained with a Cary Eclipse spectrofluorometer, equipped with a Cary Peltier temperature control accessory. Fluorescence spectra were recorded at 25 °C in a 3 mL quartz cuvette with 1 cm path length, using emission slits of 5 nm. An excitation wavelength of 295 nm was used in order to specifically excite tryptophan residues, while emission was scanned in the range 300 to 600 nm. Protein concentration was 5 μM in 50 mM Tris-HCl, pH 7.2, 0.2 M NaCl. Notably, following long-term exposure of the protein to MG, in the order of 30 to 60 min, a brown color developed, presumably due to oxidative damage of the protein. Therefore, all assays with MG were conducted with freshly prepared reagents within 5 min, while keeping all reagents on ice until used. Titrations were performed with freshly prepared 10–100 mM stock solutions of glutathione, methylglyoxal, and $CoCl_2$, in the same buffer; which were kept on ice throughout the assays. Volume corrections were applied to all titration spectra. Fluorescence quenching data were expressed as Stern–Volmer plots, modeling the ratio of initial to final fluorescence, F_0/F, as a linear function of the quencher concentration [Q], where the slope is the quenching constant $1/K_{SV}$, that is $F_0/F - 1 = (F_0-F)/F = [Q]/K_{SV}$. If the quenching mechanism is static, K_{SV} represents the dissociation constant of the fluorescent complex.

Acknowledgements

We are grateful for access to the PROXIMA-2A beamline at Synchrotron SOLEIL (France), and Daniela Albanesi for her help with protein crystallization. This work was supported by funds from CONICET (Argentinian Research Council), and ANPCyT (Agency for Science and Technology Promotion), grants PICT 2010-0358 to V. A. C-B. and PICT 2017-4590 to J. M. G.

Conflict of interest

The authors declare no conflict of interest.

Author contributions

RBA cloned and purified the proteins. CEA and SK crystallized and solved structures. JMG designed and performed fluorescence assays, interpreted crystal structures, and wrote the manuscript. VAC-B and CSA designed the experiments and wrote the manuscript.

References

1 Phillips SA & Thornalley PJ (1993) The formation of methylglyoxal from triose phosphates: investigation using a specific assay for methylglyoxal. *Eur J Biochem* **212**, 101–105.
2 Chen M & Thelen JJ (2010) The plastid isoform of triose phosphate isomerase is required for the postgerminative

transition from heterotrophic to autotrophic growth in Arabidopsis. *Plant Cell* **22**, 77–90.
3 Richard JP (1991) Kinetic parameters for the elimination reaction catalyzed by triosephosphate isomerase and an estimation of the reaction's physiological significance. *Biochemistry* **30**, 4581–4585.
4 Martins AM, Mendes P, Cordeiro C & Freire AP (2001) In situ kinetic analysis of glyoxalase I and glyoxalase II in *Saccharomyces cerevisiae*. *Eur J Biochem* **268**, 3930–3936.
5 Aldini G, Vistoli G, Stefek M, Chondrogianni N, Grune T, Sereikaite J, Sadowska-Bartosz I & Bartosz G (2013) Molecular strategies to prevent, inhibit, and degrade advanced glycoxidation and advanced lipoxidation end products. *Free Radical Res* **47**, 93–137.
6 Lee AT, Plump A, DeSimone C, Cerami A & Bucala R (1995) A role for DNA mutations in diabetes-associated teratogenesis in transgenic embryos. *Diabetes* **44**, 20–24.
7 Murata-Kamiya N, Kamiya H, Kaji H & Kasai H (2000) Methylglyoxal induces G: C to C: G and G: C to T: a transversions in the supF gene on a shuttle vector plasmid replicated in mammalian cells. *Mutat Res/ Genetic Toxicol Environment Mutag* **468**, 173–182.
8 Sibbersen C, Palmfeldt J, Hansen J, Gregersen N, Jørgensen KA & Johannsen M (2013) Development of a chemical probe for identifying protein targets of α-oxoaldehydes. *Chem Commun* **49**, 4012–4014.
9 Ghosh A, Kushwaha HR, Hasan MR, Pareek A, Sopory SK & Singla-Pareek SL (2016) Presence of unique glyoxalase III proteins in plants indicates the existence of shorter route for methylglyoxal detoxification. *Sci Rep* **6**, 18358.
10 Racker E (1951) The mechanism of action of glyoxalase. *J Biol Chem* **190**, 685–696.
11 Thornalley PJ (1990) The glyoxalase system: new developments towards functional characterization of a metabolic pathway fundamental to biological life. *Biochem J* **269**, 1–11.
12 McLellan AC & Thornalley PJ (1989) Glyoxalase activity in human red blood cells fractioned by age. *Mech Ageing Dev* **48**, 63–71.
13 Rabbani N & Thornalley PJ (2011) The glyoxalase system – from microbial metabolism, through ageing to human disease and multidrug resistance. *Semin Cell Dev Biol* **22**, 261.
14 Rabbani N & Thornalley PJ (2014) The critical role of methylglyoxal and glyoxalase 1 in diabetic nephropathy. *Diabetes* **63**, 50–52.
15 Takagi D, Inoue H, Odawara M, Shimakawa G & Miyake C (2014) The Calvin cycle inevitably produces sugar-derived reactive carbonyl methylglyoxal during photosynthesis: a potential cause of plant diabetes. *Plant Cell Physiol* **55**, 333–340.
16 Smits MM & Johnson MA (1981) Methylglyoxal: enzyme distributions relative to its presence in Douglas-fir needles and absence in Douglas-fir needle callus. *Arch Biochem Biophys* **208**, 431–439.
17 Talesa V, Rosi G, Contenti S, Mangiabene C, Lupattelli M, Norton S, Giovannini E & Principato G (1990) Presence of glyoxalase II in mitochondria from spinach leaves: comparison with the enzyme from cytosol. *Biochem Int* **22**, 1115–1120.
18 Norton S, Talesa V, Yuan W & Principato G (1990) Glyoxalase I and glyoxalase II from Aloe vera: purification, characterization and comparison with animal glyoxalases. *Biochem Int* **22**, 411–418.
19 Deswal R, Chakaravarty T & Sopory S (1993) The glyoxalase system in higher plants: regulation in growth and differentiation. *Biochem Soc Trans* **21**, 527–530.
20 Paulus C, Köllner B & Jacobsen H-J (1993) Physiological and biochemical characterization of glyoxalase I, a general marker for cell proliferation, from a soybean cell suspension. *Planta* **189**, 561–566.
21 Chakravarty T & Sopory S (1998) Blue light stimulation of cell proliferation and glyoxalase I activity in callus cultures of *Amaranthus paniculatus*. *Plant Sci* **132**, 63–69.
22 Kaur C, Ghosh A, Pareek A, Sopory SK & Singla-Pareek SL (2014) Glyoxalases and stress tolerance in plants. *Biochem Soc Trans* **42**, 485–490.
23 Turra GL, Agostini RB, Fauguel CM, Presello DA, Andreo CS, González JM & Campos-Bermudez VA (2015) Structure of the novel monomeric glyoxalase I from Zea mays. *Acta Crystallogr D Biol Crystallogr* **71**, 2009–2020.
24 Cameron AD, Olin B, Ridderström M, Mannervik B & Jones TA (1997) Crystal structure of human glyoxalase I—evidence for gene duplication and 3D domain swapping. *EMBO J* **16**, 3386–3395.
25 Suttisansanee U & Honek JF (2011) Bacterial glyoxalase enzymes. *Semin Cell Dev Biol* **22**, 285–292.
26 Sukdeo N & Honek JF (2007) Pseudomonas aeruginosa contains multiple glyoxalase I-encoding genes from both metal activation classes. *Biochim Biophys Acta (BBA)-Proteins Proteomics* **1774**, 756–763.
27 Mustafiz A, Ghosh A, Tripathi AK, Kaur C, Ganguly AK, Bhavesh NS, Tripathi JK, Pareek A, Sopory SK & Singla-Pareek SL (2014) A unique Ni^{2+}-dependent and methylglyoxal-inducible rice glyoxalase I possesses a single active site and functions in abiotic stress response. *Plant J* **78**, 951–963.
28 Jain M, Batth R, Kumari S & Mustafiz A (2016) Arabidopsis thaliana contains both Ni^{2+} and Zn^{2+} dependent glyoxalase I enzymes and ectopic expression of the latter contributes more towards abiotic stress tolerance in *E. coli*. *PLoS ONE* **11**, e0159348.
29 He MM, Clugston SL, Honek JF & Matthews BW (2000) Determination of the structure of *Escherichia coli* glyoxalase I suggests a structural basis for differential metal activation. *Biochemistry* **39**, 8719–8727.

30 Suttisansanee U, Lau K, Lagishetty S, Rao KN, Swaminathan S, Sauder JM, Burley SK & Honek JF (2011) Structural variation in bacterial glyoxalase I enzymes: investigation of the metalloenzyme glyoxalase I from *Clostridium acetobutylicum*. *J Biol Chem* **286**, 38367–38374.
31 Marmstål E, Aronsson A-C & Mannervik B (1979) Comparison of glyoxalase I purified from yeast (*Saccharomyces cerevisiae*) with the enzyme from mammalian sources. *Biochem J* **183**, 23–30.
32 Iozef R, Rahlfs S, Chang T, Schirmer H & Becker K (2003) Glyoxalase I of the malarial parasite *Plasmodium falciparum*: evidence for subunit fusion. *FEBS Lett* **554**, 284–288.
33 Rae C, Berners-Price SJ, Bulliman BT & Kuchel PW (1990) Kinetic analysis of the human erythrocyte glyoxalase system using ^{1}H NMR and a computer model. *Eur J Biochem* **193**, 83–90.
34 Deponte M, Sturm N, Mittler S, Harner M, Mack H & Becker K (2007) Allosteric coupling of two different functional active sites in monomeric *Plasmodium falciparum* glyoxalase I. *J Biol Chem* **282**, 28419–28430.
35 Bythell-Douglas R, Suttisansanee U, Flematti GR, Challenor M, Lee M, Panjikar S, Honek JF & Bond CS (2015) The crystal structure of a homodimeric *Pseudomonas* glyoxalase I enzyme reveals asymmetric metallation commensurate with half-of-sites activity. *Chem–A European J* **21**, 541–544.
36 Clugston SL, Yajima R & Honek JF (2004) Investigation of metal binding and activation of *Escherichia coli* glyoxalase I: kinetic, thermodynamic and mutagenesis studies. *Biochem J* **377**, 309–316.
37 Ridderström M, Cameron AD, Jones TA & Mannervik B (1998) Involvement of an active-site Zn^{2+} ligand in the catalytic mechanism of human glyoxalase I. *J Biol Chem* **273**, 21623–21628.
38 Sellin S, Eriksson LE, Aronsson AC & Mannervik B (1983) Octahedral metal coordination in the active site of glyoxalase I as evidenced by the properties of Co(II)-glyoxalase I. *J Biol Chem* **258**, 2091–2093.
39 Mannervik B, Aronsson AC, Marmstal E & Tibbelin G (1981) Glyoxalase I (rat liver). *Methods Enzymol* **77**, 297–301.
40 Bliven S, Lafita A, Parker A, Capitani G & Duarte JM (2018) Automated evaluation of quaternary structures from protein crystals. *PLoS Comput Biol* **14**, e1006104.
41 Cameron AD, Ridderström M, Olin B, Kavarana MJ, Creighton DJ & Mannervik B (1999) Reaction mechanism of glyoxalase I explored by an X-ray crystallographic analysis of the human enzyme in complex with a transition state analogue. *Biochemistry* **38**, 13480–13490.
42 Vander Jagt DL, Han LP & Lehman CH (1972) Kinetic evaluation of substrate specificity in the glyoxalase-I-catalyzed disproportionation of α-ketoaldehydes. *Biochemistry* **11**, 3735–3740.
43 Garcia-Iniguez L, Powers L, Chance B, Sellin S, Mannervik B & Mildvan AS (1984) X-ray absorption studies of the Zn^{2+} site of glyoxalase I. *Biochemistry* **23**, 685–689.
44 Su Z, Sukdeo N & Honek JF (2008) ^{15}N–^{1}H HSQC NMR Evidence for distinct specificity of two active sites in *Escherichia coli* glyoxalase I. *Biochemistry* **47**, 13232–13241.
45 Lages NF, Cordeiro C, Silva MS, Freire AP & Ferreira AE (2012) Optimization of time-course experiments for kinetic model discrimination. *PLoS ONE* **7**, e32749.
46 Landro JA, Brush EJ & Kozarich JW (1992) Isomerization of (*R*)- and (*S*)- glutathiolactaldehydes by glyoxalase I: the case for dichotomous stereochemical behavior in a single active site. *Biochemistry* **31**, 6069–6077.
47 Tyagi R, Lai R & Duggleby RG (2004) A new approach to 'megaprimer' polymerase chain reaction mutagenesis without an intermediate gel purification step. *BMC Biotechnol* **4**, 2.
48 Studier FW (2005) Protein production by auto-induction in high-density shaking cultures. *Protein Expr Purif* **41**, 207–234.
49 Gill SC & Von Hippel PH (1989) Calculation of protein extinction coefficients from amino acid sequence data. *Anal Biochem* **182**, 319–326.
50 Bradford MM (1976) A rapid and sensitive method for the quantitation of microgram quantities of protein utilizing the principle of protein-dye binding. *Anal Biochem* **72**, 248–254.
51 Ridderström M & Mannervik B (1996) The primary structure of monomeric yeast glyoxalase I indicates a gene duplication resulting in two similar segments homologous with the subunit of dimeric human glyoxalase I. *Biochem J* **316**, 1005–1006.
52 Kabsch W (2010) Integration, scaling, space-group assignment and post-refinement. *Acta Crystallogr D Biol Crystallogr* **66**, 133–144.
53 McCoy AJ, Grosse-Kunstleve RW, Adams PD, Winn MD, Storoni LC & Read RJ (2007) Phaser crystallographic software. *J Appl Crystallogr* **40**, 658–674.
54 Murshudov GN, Vagin AA & Dodson EJ (1997) Refinement of macromolecular structures by the maximum-likelihood method. *Acta Crystallogr D Biol Crystallogr* **53**, 240–255.
55 Collaborative Computational Project, N (1994) The CCP4 suite: programs for Protein Crystallography. *Acta Crystallogr D Biol Crystallogr* **50**, 760–763.

56 Emsley P, Lohkamp B, Scott WG & Cowtan K (2010) Features and development of Coot. *Acta Crystallogr D Biol Crystallogr* **66**, 486–501.

57 Chen VB, Arendall WB 3rd, Headd JJ, Keedy DA, Immormino RM, Kapral GJ, Murray LW, Richardson JS & Richardson DC (2010) MolProbity: all-atom structure validation for macromolecular crystallography. *Acta Crystallogr D Biol Crystallogr* **66**, 12–21.

58 Westbrook J, Feng Z, Burkhardt K & Berman HM (2003) Validation of protein structures for protein data bank. *Methods Enzymol* **374**, 370–385.

59 Pavelka A, Šebestová E, Kozlíková B, Brezovský J, Sochor J & Damborský J (2016) CAVER: Algorithms for analyzing dynamics of tunnels in macromolecules. *IEEE/ACM Trans Comput Biol Bioinf* **13**, 505–517.